 doi:10.20944/preprints202202.0040.v1

Preparation of Ti-46Al-8Nb Alloy Ingots beyond Laboratory Scale Based on $BaZrO_3$ Refractory Crucible

Baohua Duan[a], Lu Mao[a], Yuchen Yang[a], Qisheng Feng[a], Xuexian Zhang[a], Haitao Li[a], Lina Jiao[a], Rulin Zhang[a,c], Xionggang Lu[a,b,c], Guangyao Chen[a,b*], Chonghe Li[a,b*]

[a] State Key Laboratory of Advanced Special Steel & Shanghai Key Laboratory of Advanced Ferrometallurgy & School of Materials Science and Engineering, Shanghai University, Shanghai 200072, China

[b] Shanghai Special Casting Engineering Technology Research Center, Shanghai 201605, China

[c] Shanghai DianJi University, Shanghai 201306, China

[*] Corresponding Author:

Chonghe Li: chli@staff.shu.edu.cn; Guangyao Chen: cgybless1@shu.edu.cn. Shanghai Special Casting engineering technology research center, School of Materials Science and Engineering, Shanghai University, Shanghai, 200444, P.R. China

Abstract

The high Nb-containing TiAl-based alloy ingot beyond laboratory scale with a composition of Ti-46Al-8Nb (at. %) was prepared by a vacuum induction melting process based on $BaZrO_3$ refractory. An ingot without macroscopic casting defects (such as pipe shrinkage and center line porosity) was finally obtained, and the chemical composition, solidification path, microstructure and tensile properties of the ingots were investigated. The results show that the deviations of Al and Nb content along a 430 mm long central part of the ingot are approximately ±0.39 at. % and ±0.14 at. %, and the oxygen content in the ingot can be controlled at around 1000 ppm. During the solidification process, the alloy suffered from peritectic reaction and formed columnar grains with anisotropy. In addition to Al segregation and Nb segregation, β-phase particles associated with γ phase at the triple junction of the colonies were observed.

 doi:10.20944/preprints202202.0040.v1

Moreover, the mechanical properties of the ingot in the transverse direction are significantly better than those in the longitudinal direction, with a tensile strength of up to high as 700 MPa and a corresponding fracture elongation of 1.1 %.

Keywords: Ti-46Al-8Nb alloy, Vacuum induction melting, $BaZrO_3$ refractory, Microsegregation, Mechanical properties

1. Introduction

TiAl-based alloy, mainly composed of γ (TiAl) and α_2 (Ti_3Al) intermetallic compounds, has a density of about 3.9~4.2 g/cm^3, and has a very broad application prospect in aerospace, automobile manufacturing and other fields due to its excellent high temperature performance [1-3]. Particularly in the temperature range of 600~800 ℃, TiAl-based alloy exhibits a comparable or better specific yield strength than the currently used nickel-based superalloy in aeroengine blades [4].

From the view of adding the third element, Nb and several other elements have a significant impact on the oxidation resistance of TiAl-based alloy. High Nb-containing TiAl-based alloys are expected can be used between 800 ℃ and 900 ℃. However, addition of high Nb content also raises the melting point of the alloy, making more difficult to melt and prepare the alloy. Therefore, it is of great significance to explore the melting process of the high Nb-containing TiAl-based alloy [5-7].

At present, the three main melting techniques that have been used to produce TiAl ingots on an industrial basis are vacuum arc melting/remelting (VAR), plasma-arcmelting (PAM) and induction skull melting (ISM) [8]. It should be mentioned that the electron-beam melting techniques (EBM) sometimes used for melt titanium alloys are not suitable for the production of TiAl ingots because control of the aluminum

 doi:10.20944/preprints202202.0040.v1

content is very difficult due to its vaporization during the melting process. With regard to VAR technique, one of the main advantages is that the highest purity TiAl ingots can be obtained as multiple remelting. Nonetheless, the melting and solidification processes of VAR are confined in a small molten pool, thus giving a poor chemical homogeneity to the ingot [9]. Moreover, refractory particles and Ti-rich inclusions are also difficult to avoid in TiAl ingots prepared by VAR. In contrast, with PAM technique, as a consequence of the molten metal passing over the copper hearth, any high-density inclusions can fall to the bottom of the hearth melt pool, which results in them not being present in the final ingot. However, PAM technique still does not solve the problem of chemical inhomogeneity well, requiring double or even triple melting to effectively reach the expected level of ingot homogeneity, which undoubtedly increases the cost of preparation. Fortunately, this challenge is well overcome by ISM technique, which ensures good chemical homogeneity within the ingot through the intense stirring of the melt by an induced magnetic field. Additionally, the ISM method is a clean, relatively inexpensive technique that is very flexible in terms of alloy composition. Nevertheless, a main disadvantage of ISM is the limited superheat that is developed within the melt. Although high-power ISM (also known as levitation melting) allows the melt to be levitated (pushed) away from the crucible wall, increasing the superheat to 60~70 °C by reducing the crucible-melt contact [10], this means higher energy consumption and limited melt capacity (approximately a few kilograms). As a matter of fact, all the above three melting techniques utilize water-cooled copper as the crucible, which more or less cause the problem of insufficient melt superheat in the contact area between the melt

Preprints (www.preprints.org) | NOT PEER-REVIEWED | Posted: 2 February 2022 doi:10.20944/preprints202202.0040.v1

and the crucible wall. The temperature differences (low melt superheat near the crucible wall and high melt superheat away from the crucible wall) in different areas inside the molten pool may lead to chemical inhomogeneity, microstructural segregation and casting defects such as pipe shrinkage that are present in the ingot cannot be removed by subsequent hot extrusion and isothermal forging [11]. Therefore, selecting a stable and inert refractory for TiAl-based alloy melting can avoid the problem of insufficient superheat, however, this is not an easy task by considering the activity of TiAl melt.

Even though the casting method using refractory containing TiAl-based alloy melt inevitably brings about the problem of foreign element contamination, considering its cheap cost, simple operation, advantages of ensuring melt chemical homogeneity, ability to maintain melt superheat as well as industrial-scale production capacity, which remains an extremely commercially promising approach. For this reason, in the past two decades, various refractories such as oxides (Al_2O_3, CaO, ZrO_2, Y_2O_3, $CaZrO_3$, $BaZrO_3$) [12-18], carbides (graphite) [19], nitrides (AlN) [20], silicide (Mullite, SiO_2) [17, 21] and boride (BN) [20] have been extensively evaluated, and two kinds of refractories, Y_2O_3 and $BaZrO_3$, are currently used successfully. Our research group has done a lot of work on $BaZrO_3$ series perovskite refractories used in Ti alloys melting, and the results show that $BaZrO_3$ series perovskite refractories have excellent corrosion resistance to Ti alloy melt [15, 16, 22, 23]. However, the use of $BaZrO_3$ refractories to produce TiAl-based alloy ingots beyond laboratory scale has not yet been reported.

Based on the above review, in this paper, $BaZrO_3$ refractory crucible combined with vacuum induction melting (hereinafter referred to as VIM-BZO) technique have

Preprints (www.preprints.org) | NOT PEER-REVIEWED | Posted: 2 February 2022 doi:10.20944/preprints202202.0040.v1

been used to produce Ti-46Al-8Nb (at. %) alloy ingot with large size (10 kg). Compared with the small ingot of the experimental scale, the chemical composition and microstructure of the large ingot are more uniform, and its performance is more representative. In addition, it is of great significance to study the microstructure and properties of large ingots for the industrial production of TiAl-based alloys.

2. Experimental Method and Procedure

2.1 Melting process

The ingots with the composition of Ti-46Al-8Nb (at. %) were prepared by vacuum induction melting (VIM) in a 25 Kg-grade in-house U-shaped laboratory-scale $BaZrO_3$ crucible. The details preparation process of the $BaZrO_3$ crucible can be referred to the previous work of our research group [24], a simple schematic process is shown in Fig. 1. Pure titanium sponge (99.97 %), high-purity aluminum ingots (99.99 %) and an Al-60Nb (wt. %) intermediate alloy were used as experimental raw materials. Before feeding, the raw materials must be baked at 150°C for 2 hours in a drying oven to fully evaporate the water. Before the heating cycle, the furnace was evacuated up to less than 0.03 Pa by a diffusion pump, and then backfilled three times with purity argon (99%) in order to minimize the hydrosphere and oxygen content. When the raw material start melting, the furnace was backfilled with purity argon to 0.4 MPa to prevent the evaporation of aluminum. Fig. 2 shows a step diagram of the melting process, including the heating power and the required holding time. After the raw material completely melted, the molten metal was poured into a graphite mold with a size of Φ85 mm × 600 mm to obtain a high-Nb containing TiAl-based alloy ingot. The melting temperature

Preprints (www.preprints.org) | NOT PEER-REVIEWED | Posted: 2 February 2022 doi:10.20944/preprints202202.0040.v1

was monitored by KB-602 thermocouple and Marathon series dual-color integrated infrared thermometer.

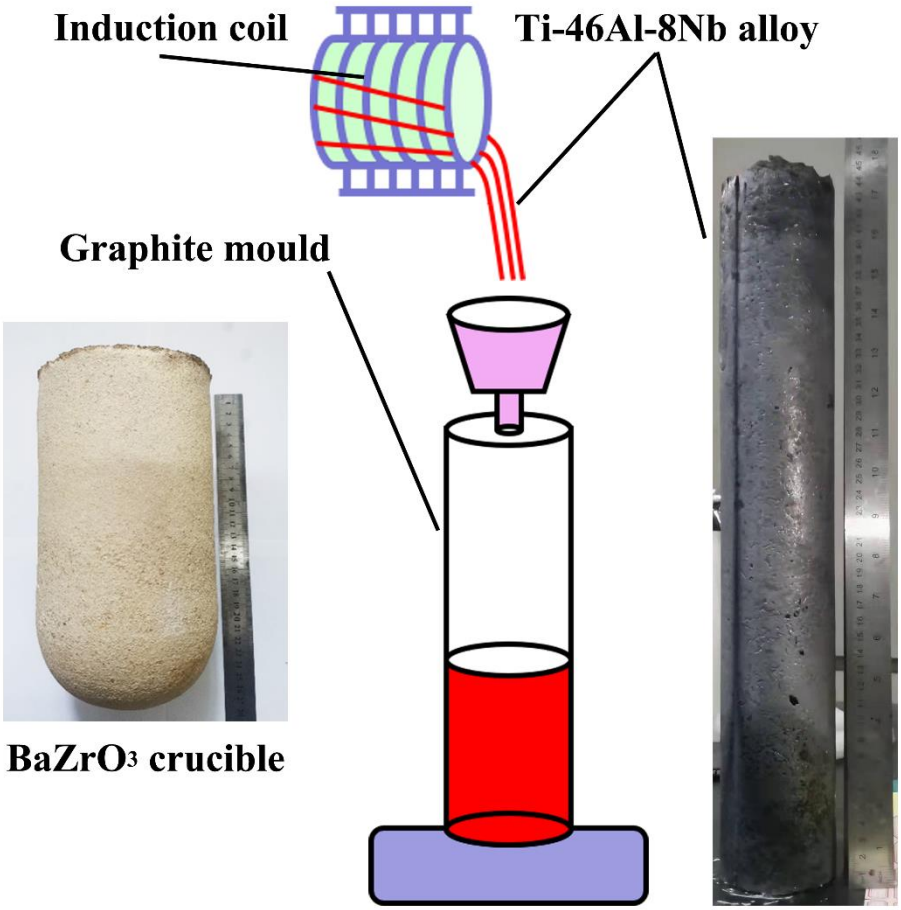

Fig. 1 Schematic diagram of the Ti-46Al-8Nb alloy melting process.

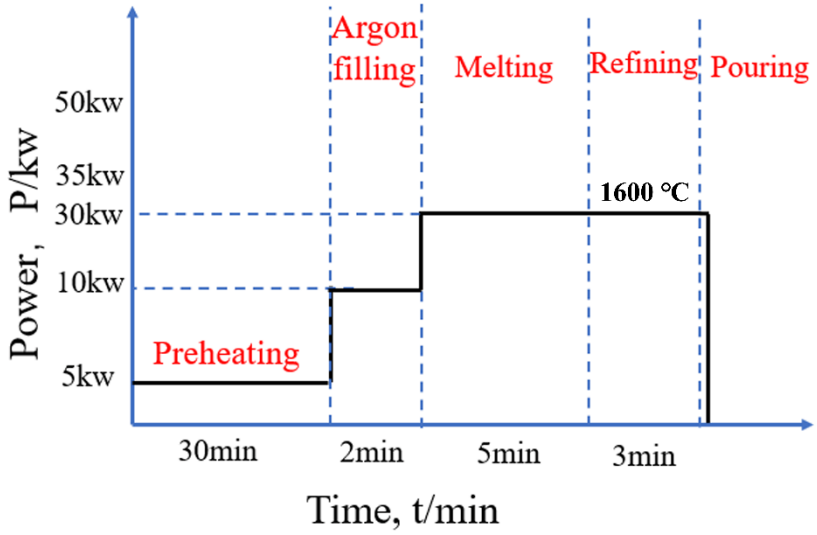

Fig.2 The melting power and corresponding holding time.

Preprints (www.preprints.org) | NOT PEER-REVIEWED | Posted: 2 February 2022 doi:10.20944/preprints202202.0040.v1

2.2 Sampling and processing

The cutting and sampling of the ingot are shown in Fig. 3. The 2 mm thin slice was cut along the center of the ingot by wire electrical discharge machine (WEDM-M332), as shown in Fig. 3a, and then the required samples were obtained from the thin slice, as shown in Fig. 3b, and the size of the tensile specimen was shown in Fig. 3c. The metallographic samples were processed by standard metallographic techniques, first smoothed on sandpaper, then polished with silica suspension (particle size: 0.25 μm), and etched in corrosive agent (H2O: HNO3: HF= 18:1:1) for 10 seconds.

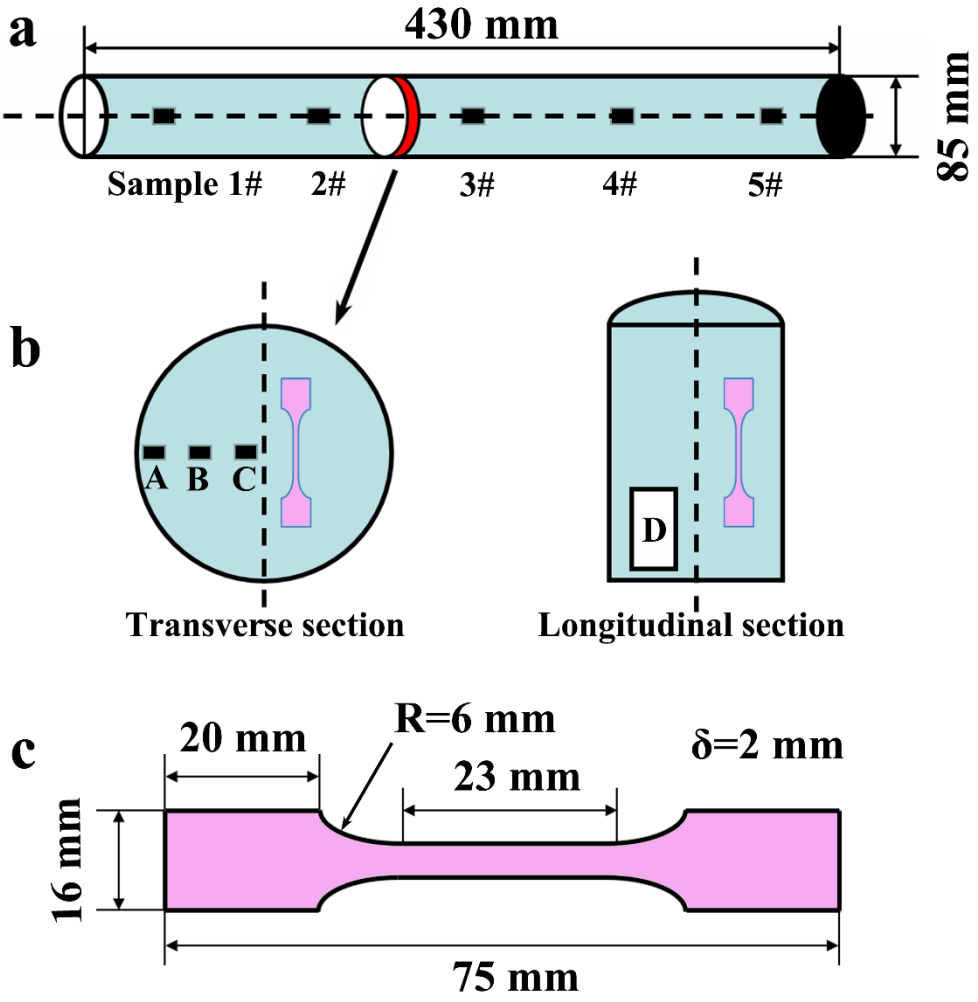

Fig. 3 Schematic diagram of sampling.

Preprints (www.preprints.org) | NOT PEER-REVIEWED | Posted: 2 February 2022 doi:10.20944/preprints202202.0040.v1

2.3 Sample characterization and testing

The microstructure of the ingots was characterized by LEICA metallographic microscope and JSM-6700F scanning electron microscope (SEM). Point and line scanning analysis for the alloy ingot through an energy dispersive spectrometer (EDS). The oxygen content and chemical composition of the ingots were measured by pulse heating inert gas melting infrared absorption method (TC-436 Nitrogen and oxygen analyzer) and inductively coupled plasma optical emission spectrometry (ICP-OES), respectively. The phases of the samples were identified using an X-ray diffractometer (D/Max-2200). The tensile properties of the samples were tested using a Zwick (CMT-100) universal testing machine.

3. Results and discussions

3.1 Chemical composition and phases

Since the VIM-BZO technique is used in this study, strong electromagnetic stirring and sufficient superheating can ensure a relatively good chemical homogeneity of the ingot. Analyzing the chemical composition of the ingot, as shown in Table 1, it can be seen that the deviations of Al and Nb content along a 430 mm long central part of the ingot are approximately ±0.39 at. % and ±0.14 at. %. Compared with the double-melted VAR large ingot (±0.7 at. % Al) [25], the double-melted PAM large ingots (±0.5 at. % Al) [26] and the single-melted ISM large ingot (±0.75 at. % Al) [27], the deviation of Al content of the single-melted VIM-BZO large ingot in this study is undoubtedly encouraging. Overall, the Al content is slightly lower than the nominal level, which is caused by the evaporation of Al during the melting process, even though 0.6 wt.% Al

Preprints (www.preprints.org) | NOT PEER-REVIEWED | Posted: 2 February 2022 doi:10.20944/preprints202202.0040.v1

has been compensated for during batching. The contaminating element O mainly comes from the $BaZrO_3$ refractory crucible. It can be seen that the oxygen content of the ingot prepared using the $BaZrO_3$ refractory crucible is slightly less than twice that of the water-cooled copper crucible (about 500~600 ppm) [28].

Table 1 Chemical composition of the produced Ti-46Al-8Nb alloy ingots.

Elements	Al (at. %)		Nb (at. %)		O (ppm)	Ti (at. %)
Sample 1#	45.01		7.97		1053	Bal.
Sample 2#	45.40		7.90		991	Bal.
Sample 3#	45.32		7.75		975	Bal.
Sample 4#	45.53		7.84		1021	Bal.
Sample 5#	45.76		7.98		1047	Bal.
Deviation	$\bar{x}$-x_{min} +0.39	$\bar{x}$-x_{max} -0.36	$\bar{x}$-x_{min} +0.14	$\bar{x}$-x_{max} -0.09	/	/
Target	46		8		/	Bal.

Note: the oxygen content in the raw material is about 150 ppm (mass fraction).

A detailed evaluation of the Ti-Al-Nb ternary system was carried out by Witusiewicz et al. [29] in 2009 and the corresponding TDB file is attached. After analyzing their data in detail, this study used their database as a standard and utilized Pandat software to describe the Ti-Al pseudo-binary phase diagram with 8 at. % Nb concentration, as shown in Fig. 4. The Ti-Al-Nb ternary phase diagram evaluated by Witusiewicz et al. indicates that the Ti-46Al-8Nb alloy is mainly composed of γ (TiAl), α_2 (Ti_3Al) and β_o (bcc-B2) phases at room temperature [29]. However, the X-ray diffraction spectra showed that there were only two phases, γ and α_2, in the ingot, as shown in Figure 5, which may be due to the fact that the content of β phase is too small to exceed the minimum standard that can be detected by the instrument.

Preprints (www.preprints.org) | NOT PEER-REVIEWED | Posted: 2 February 2022 doi:10.20944/preprints202202.0040.v1

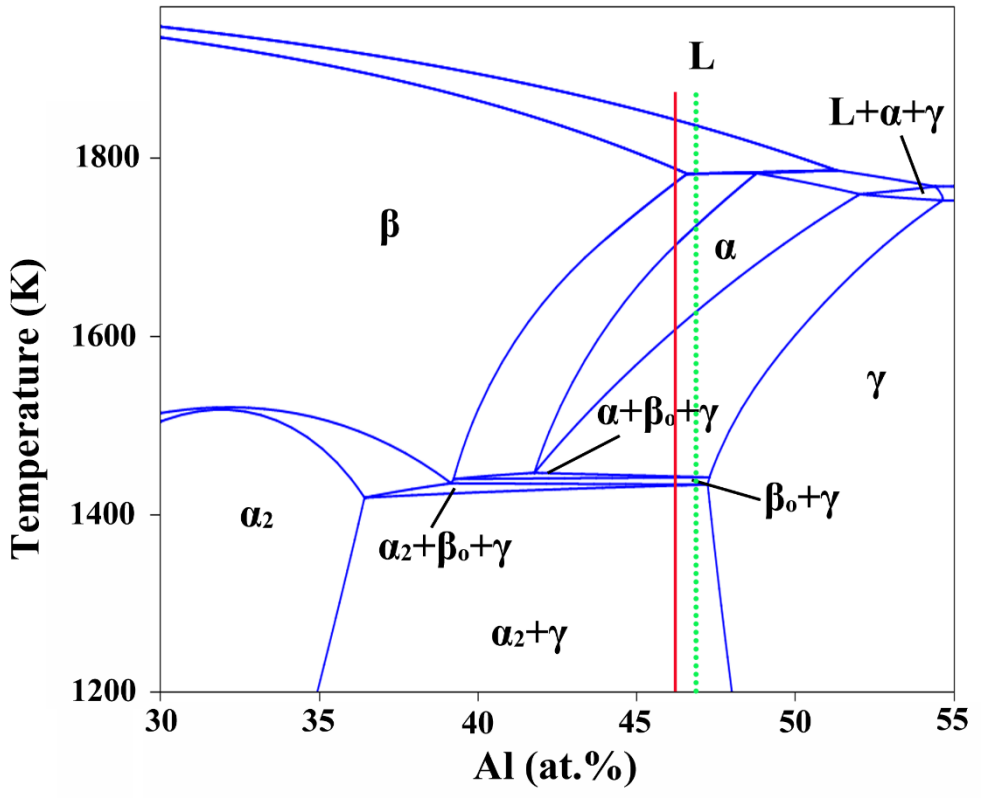

Fig. 4 Pseudo-binary phase diagram of Ti-Al with 8 at. % Nb concentration [29].

In addition, according to the peak intensity analysis of X-ray diffraction pattern, γ phase is the main phase in the alloy ingot. However, the α_2 phase content of sample A near the surface of the ingot is significantly higher than that of sample B in the middle region and sample C in the core, and shows a decreasing relationship. This is mainly due to the fact that the pre-solidified area of the ingot surface contains more high melting point Ti and Nb elements, so that the final solidified core area is rich in Al element. As a result, the content of α_2 phase is higher on the ingot surface, while the content of γ phase in the core is increased.

Preprints (www.preprints.org) | NOT PEER-REVIEWED | Posted: 2 February 2022 doi:10.20944/preprints202202.0040.v1

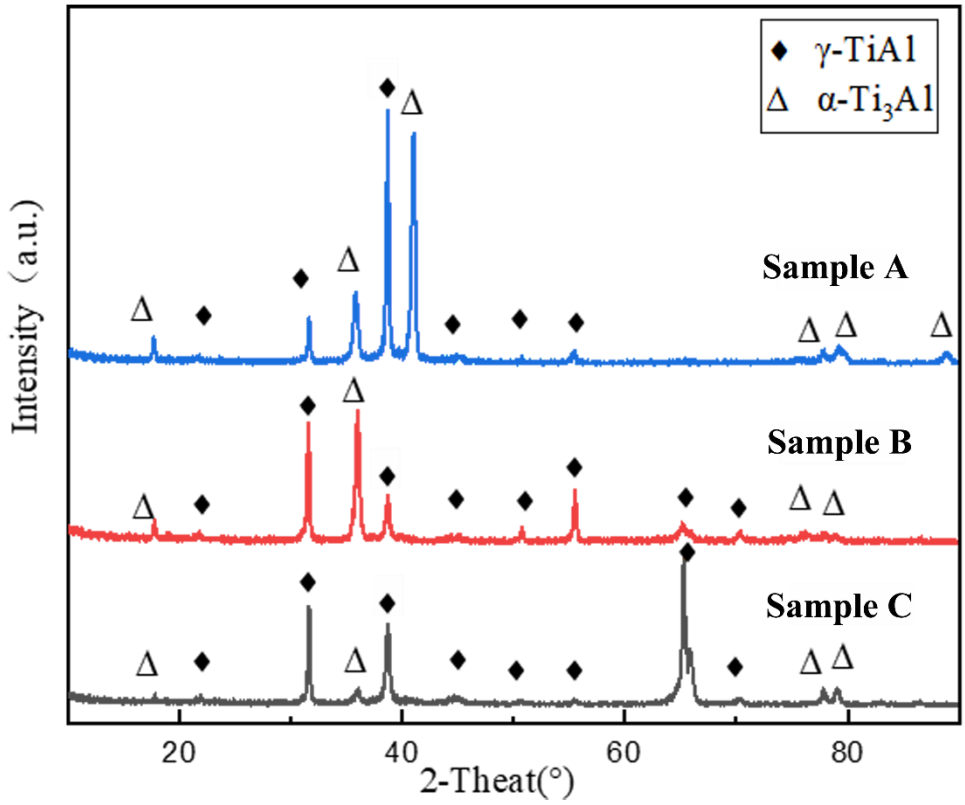

Fig. 5 X-ray diffraction spectra of the ingot obtained at different location. The locations of samples A, B and C are shown in Fig. 3.

3.2 Structure and microsegregation

In order to investigate the structure of the Ti-46Al-8Nb alloy ingot prepared by the VIM-BZO technique, the transverse section and longitudinal section of the ingot were analyzed in detail in this study, and the sampling schematic diagram is shown in Fig. 3. First, analyzing the transverse section, as shown in Fig. 6, the macrostructure shows that the columnar grains with a specific orientation (perpendicular to the central axis and parallel to the heat flow but in the opposite direction) are predominant in the ingot (Fig. 6a). According to previous studies [30-32], in the absence of grain-refining elements such as B, the solidification structure of TiAl-based alloys usually shows a large difference depending on whether it solidifies via the β phase (β-solidified TiAl-based alloy) or peritectic via the α phase (peritectic solidified TiAl-based alloy). β-

 doi:10.20944/preprints202202.0040.v1

solidified TiAl-based alloys exhibited structures consisting of relatively large equiaxed grains, whereas peritectic solidified TiAl-based alloys showed columnar grains that had grown in the opposite direction to that of heat flow. However, the target alloy in this study shows that it solidifies through the β phase on the phase diagram, as shown by the red solid line in Fig. 4, but the actual ingot shows the typical microstructure characteristics of the peritectic solidified TiAl-based alloys. Moreover, the actually measured Al content in the ingot is not higher than 46 at. % (Table 1). Therefore, it is believed that the actual solidification path has shifted to the high Al direction, as shown by the dotted green line in Fig. 4, which may be caused by the following two reasons: (i) Caused by the non-equilibrium solidification process; (ii) The influence of oxygen content. Oxygen is the stabilizer of the α phase, which will expand the α phase field to the low Al direction. The literature shows that 1 at. % O is about equivalent to 3.57~4.58 at. % Al in the TiAl-based alloy [33]; (iii) Since the pre-solidified β phase contains more Nb and Ti, the remaining liquid phase is locally enriched in Al. If the Al content reaches the composition range of the peritectic reaction, peritectic solidification will occur instead of β solidification.

Preprints (www.preprints.org) | NOT PEER-REVIEWED | Posted: 2 February 2022 doi:10.20944/preprints202202.0040.v1

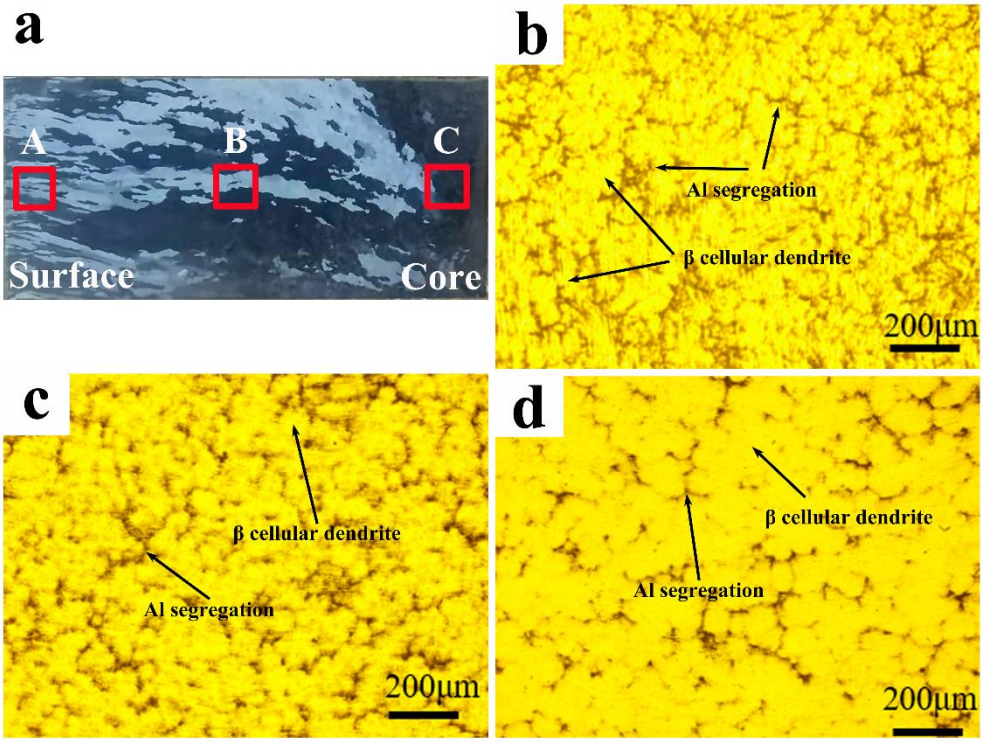

Fig. 6 Structure of the transverse section of the alloy ingot. (a) Macrograph from surface to core; (b), (c) and (d) are the metallographic structures of sample A, sample B and sample C, respectively.

In addition, the grains near the surface of the ingot are smaller than those in the core, and the closer to the core, the larger the grains. The dendritic morphologies of different regions on the transverse section are shown in Fig. 6b, c and d, it can be seen that the cellular dendrite region is bright and the interdendrite is dark in contrast. This is mainly due to the segregation of Al and Nb. As described of the phase diagram in Figure 4, the primary phase is the β phase (L → L + β), so the bright in contrast is the β cellular dendrite. When the temperature falls into the peritectic reaction, Al and Nb elements will be distinguishable redistribution redistributed through the peritectic transformation L + β → α, where Al diffuses into the α phase and the β stabilizer Nb is pushed in the opposite direction. This phenomenon is more obvious in Fig. 7a, except for the dark area of Al segregation, the "white network" inside the dendrite enveloped

Preprints (www.preprints.org) | NOT PEER-REVIEWED | Posted: 2 February 2022 doi:10.20944/preprints202202.0040.v1

by the gray area is Nb segregation. Analyzing the line scan profile of the black region, as shown in Fig. 7b, it can be clearly seen that the peak intensity of Al element in this area increases, while the peak intensity of Nb element decreases.

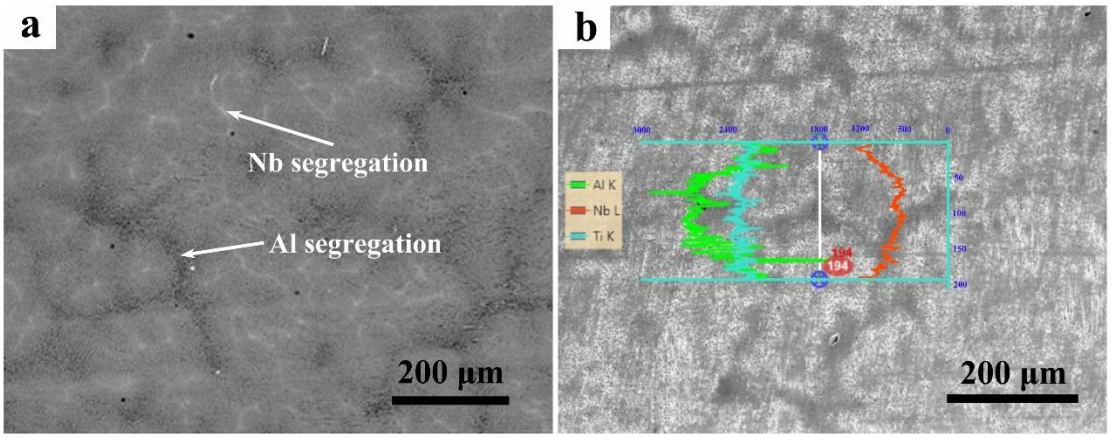

Fig. 7 Micromorphology and line scan analysis of the transverse section under SEM.

The solidification structure of the longitudinal section of the ingot was characterized, as shown in Fig. 8. At the bottom area of the ingot, since the downward direction is the main heat flow direction, and the left direction is the secondary heat flow direction, as shown by the arrows, the growth direction of the columnar grain is opposite to the heat flow direction, that is, it grows in the upper-right direction (Fig. 8a). Fig. 8b is the corresponding microstructures in the red frame of Fig. 8a. The segregation situation is similar to that of the transverse section, but the dendrite morphology in Fig. 8b is different from the transverse section, which is mainly caused by the different selected sections. It can be seen that the primary and secondary dendrite arms are about 90°, indicating that they are β dendrites, which is consistent with the conclusion given by the phase diagram (Fig. 4). Fig. 8c shows the local magnification of Fig. 8b, and it can be seen that the structure of the alloy ingot is a full lamellar structure composed of γ and α_2 phases, and the thickness of the lamellae is

Preprints (www.preprints.org) | NOT PEER-REVIEWED | Posted: 2 February 2022 doi:10.20944/preprints202202.0040.v1

approximately 0.53 μm (Eight groups of lamellae with a total of 4.2 μm).

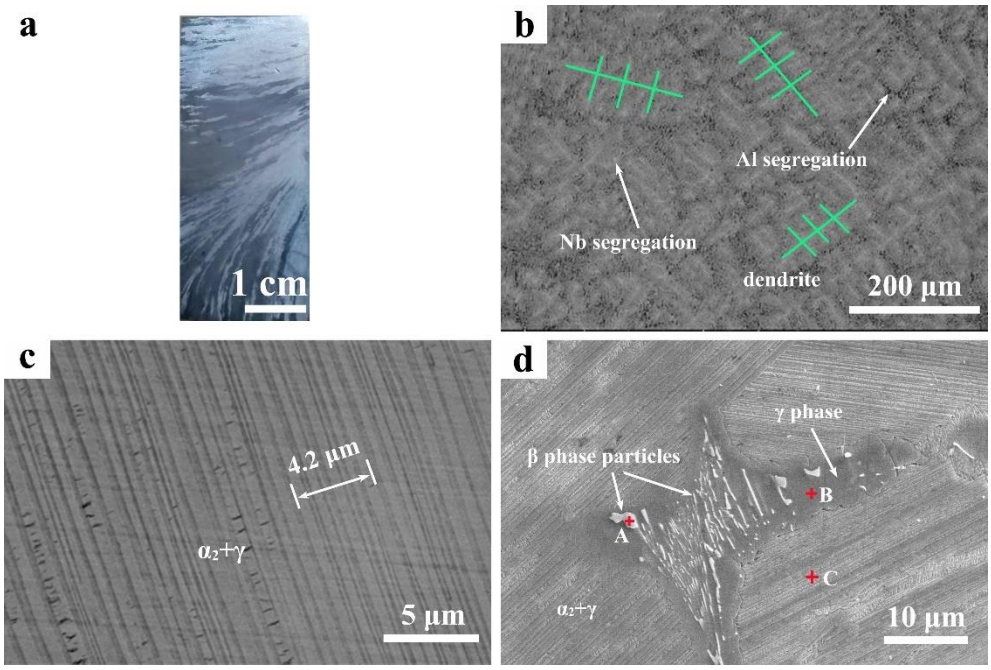

Fig. 8 Structure of the longitudinal section of the alloy ingot. (a) Macrograph of longitudinal section, and the sampling location is shown in Fig. 3; (b), (c) and (d) are the SEM diagram of longitudinal section.

Table 2 EDS analysis of the points in Fig. 8d.

Point	Unit	Element				
		Ti	Al	Nb	O	Zr
A	Wt. %	50.07	22.71	24.37	0.45	2.39
	at. %	46.71	37.62	11.72	01.27	01.17
B	Wt. %	47.86	33.50	16.13	00.30	02.20
	at. %	38.91	48.35	06.76	00.74	00.94
C	Wt. %	50.97	29.47	17.09	00.41	01.90
	at. %	44.38	45.55	07.67	01.08	00.87

In Fig. 8d, a group of white particles are aggregated at the triple conjunction of colonies, and the EDS point scan data analysis showed that the Nb content of this particle is much higher than that in the matrix (Table 2). Therefore, it is believed that these white particles are caused by Nb segregation, and the high Nb content leads to the

Preprints (www.preprints.org) | NOT PEER-REVIEWED | Posted: 2 February 2022 doi:10.20944/preprints202202.0040.v1

local area falling into the $\beta_o + \gamma + \alpha_2$ three phase field or the $\beta_o + \gamma$ two phase field, so these white particles can be considered as β_o (bcc-B2) phase. Since the β-phase particles are rich in Nb, the Al is rejected to the peripheries of the particles and surround them, forming a new phase (Fig. 8d). This phase was considered to be a γ phase by EDS analysis (Table 2).

3.3 Mechanical properties

Considering the anisotropy of ingot microstructure (as shown in Fig. 7a and Fig. 8a), in this study, the tensile properties of Ti-46Al-8Nb alloy ingot prepared by VIM-BZO technique are investigated by sampling from transverse section and longitudinal section respectively. The schematic diagram of the transverse section and longitudinal section including the microstructure is shown in Fig. 9a. Therefore, the direction of loading and stress in the transverse-cut samples are roughly consistent with the orientation of the columnar grains, while the direction of loading and stress in the longitudinal-cut samples are perpendicular to the orientation of the columnar grains. Compared with the longitudinal-cut samples, the transverse-cut samples are expected to have better mechanical properties due to the absence of transverse grain boundaries, which reduces the initiation source of microcracks. This prediction is perfectly confirmed by the tensile test, as shown in Fig. 9b, which showed that the room temperature strength of one of the transverse-cut samples is as high as 700 MPa, and the fracture elongation is 1.1 %. However, the tensile properties of the longitudinal-cut samples are significantly reduced, and one of the strength and fracture elongation are 375 MPa and 0.52 %, respectively. Fig. 9 c and d are the fracture morphologies of the

Preprints (www.preprints.org) | NOT PEER-REVIEWED | Posted: 2 February 2022 doi:10.20944/preprints202202.0040.v1

longitudinal-cut tensile sample and the transverse-cut tensile sample, respectively. A series of cleavage can be seen in the fractures in Fig. 9c and d, but the presence of dimples can also be seen in Fig. 9d. Therefore, it can be inferred that the longitudinal-cut tensile sample may be cleavage fracture, while the transverse-cut tensile sample may be quasi-cleavage fracture.

The tensile properties of the alloy ingots in this study were compared with those of high Nb-containing TiAl-based alloys prepared by different processes reported in the literature, as shown in Table 3. Both the tensile strength and the elongation of the transverse-cut samples are better than [34] that was obtained by a series of complex treatments. Xiao et al. [35] obtained an ingot with a tensile strength of 666 ± 31 MPa and a corresponding elongation of 0.56 ± 0.15 % by adding 0.15 at.% nano-Y_2O_3 particles to the alloy matrix. In comparison, the ingots obtained in one shot by the VIM-BZO technique in this study have better tensile properties in transverse section. The alloy obtained by Liu et al. [36] through a series of complex processes (PM technique to homogenize and refine microstructure, HIP technique to reduce casting defects, and HR technique to induce work hardening) has a tensile strength of 875 MPa and a corresponding elongation of 0.76 %. By contrast, the tensile strength is 175 MPa higher than that of the transverse-cut sample in this study, but the fracture elongation is 0.34 % lower.

Preprints (www.preprints.org) | NOT PEER-REVIEWED | Posted: 2 February 2022 doi:10.20944/preprints202202.0040.v1

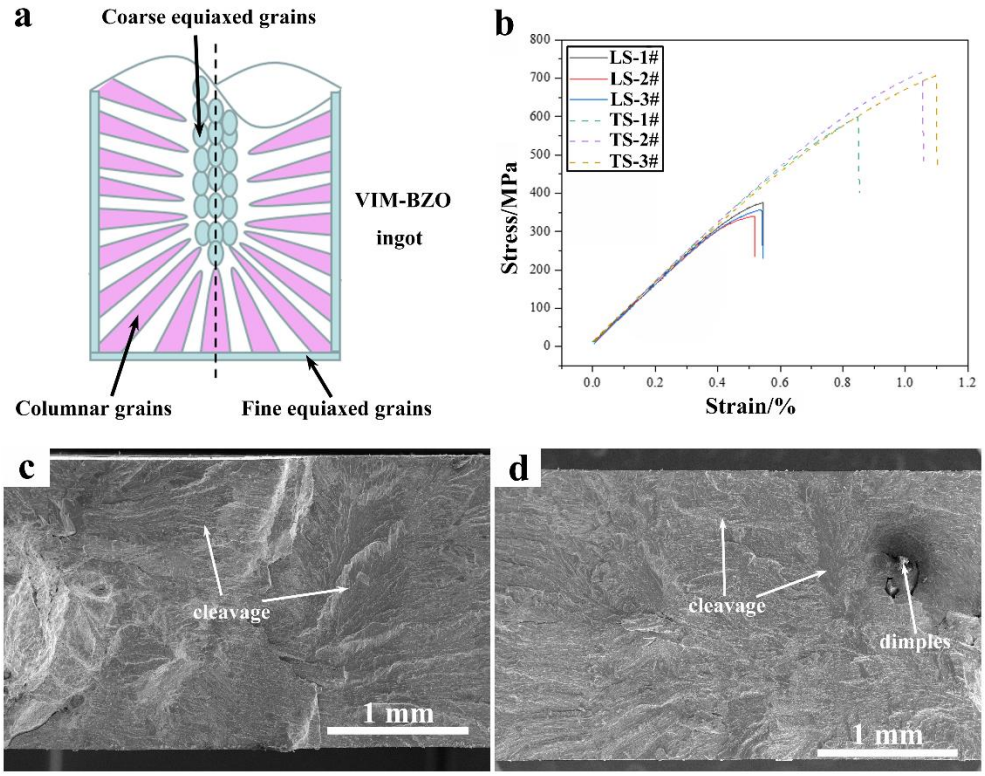

Fig. 9 Tensile properties and fracture morphologies of longitudinal and transverse sections. (a) Structural diagram of longitudinal section of the VIM-BZO alloy ingot; (b) stress-strain curve, LS: longitudinal section; TS: transverse section; (c) and (d) are the fracture morphologies of the longitudinal-cut tensile sample and the transverse-cut tensile sample, respectively.

Table 3 Room temperature mechanical properties of the high Nb containing TiAl-based alloys.

Alloys	Melting techniques	Processing techniques	Tensile strength (MPa)	Elongation (%)	references
Ti-46Al-8Nb	DM-PAM	SBQ	571 ± 18	0.43	[34]
Ti-45Al-6Nb-2.5V-0.15Y_2O_3	ISM	Casting	666 ± 31	0.56 ± 0.15	[35]
Ti-45Al-7Nb-0.3W	VAR-PM	HIP/HR	875	0.76	[36]
Ti-46Al-8Nb (longitudinal section)	VIM-BZO	Casting	700	1.1	This work
Ti-46Al-8Nb (longitudinal section)	VIM-BZO	Casting	375	0.52	This work

Note: DM (double melted); SQB (1360 ℃/1h solution treatment, then quenched into a salt bath at 850°C, finally air-cooled to room temperature); VAR-PM (The triple melting VAR ingot is used as the electrode to be atomized by the plasma rotating electrode processing to prepare the alloy powder, and then the as-prepared powder was filled into a stainless steel tank, and finally sealed and degassed at 500 °C for 12 hour, PM: powder metallurgy); HIP/HR (Hot isostatic pressing process was

Preprints (www.preprints.org) | NOT PEER-REVIEWED | Posted: 2 February 2022 doi:10.20944/preprints202202.0040.v1

conducted at a temperature of 1250 °C, pressure of 150 MPa for 5 h, then hot rolling was carried out after holding at 1280 °C for 1 hour, the rolling speed is 40 mm/s, reduction per pass is about 10%, the total reduction were 43%).

In general, VAR, ISM and PAM ingots often require very complicated subsequent processing due to their chemical inhomogeneous and casting defects, which will undoubtedly increase a lot of costs. In contrast, the ingots obtained by using the VIM-BZO technique have excellent tensile properties without subsequent processing, and this technique can also be extended to alloys of other compositions, or with some simple subsequent processing, its properties may be better, and these are exactly what needs to be done next.

4. Conclusions

In this study, Ti-46Al-8Nb alloy ingots beyond laboratory scale were prepared by vacuum induction melting technique based on a $BaZrO_3$ refractory crucible, the following conclusions can be drawn:

(1) By refining at 1600 ℃ for 3 min, a high quality and high Nb-containing TiAl-based alloy ingot with chemical homogeneity and no casting defects (such as pipe shrinkage and center line porosity) were obtained.

(2) The deviations of Al and Nb content along a 430 mm long central part of the ingot are approximately ±0.39 at. % and ±0.14 at. %, and the oxygen content in the ingot can be controlled at around 1000 ppm.

(3) During the solidification process of the alloy ingot, the primary phase is the β phase, which subsequently undergoes a peritectic reaction via the α phase instead of solidified via the β phase.

 doi:10.20944/preprints202202.0040.v1

(4) The structure of the alloy ingot is a full lamellar structure composed of γ and α_2 phases, and the thickness of the lamellae is approximately 0.53 μm. In addition, there are some Nb-rich β phase particles surrounded by γ-phase are aggregated at the triple conjunction of colonies.

(5) The tensile properties of transverse-cut samples are significantly better than those of longitudinal-cut samples, with a tensile strength of up to 700 MPa and a corresponding fracture elongation is 1.1 %.

Author Contributions: Conceptualization, Xionggang Lu; Data curation, Baohua Duan, Yuchen Yang and Rulin Zhang; Formal analysis, Baohua Duan; Funding acquisition, Chonghe Li; Investigation, Lu Mao, Yuchen Yang and Xuexian Zhang; Methodology, Lu Mao, Xuexian Zhang and Lina Jiao; Project administration, Qisheng Feng, Xionggang Lu and Guangyao Chen; Resources, Haitao Li and Lina Jiao; Software, Baohua Duan and Qisheng Feng; Supervision, Guangyao Chen and Chonghe Li; Validation, Chonghe Li; Visualization, Baohua Duan and Rulin Zhang; Writing-original draft, Baohua Duan; Writing-review & editing, Chonghe Li.

Funding: This work was supported by National Natural Science Foundation of China (Contract: U1860203); Independent Research and Development Project of State Key Laboratory of Advanced Special Steel, Shanghai Key Laboratory of Advanced Ferrometallurgy, Shanghai University (SKLASS 2020-Z11), the Science and Technology Commission of Shanghai Municipality (No. 19DZ2270200); National Natural Science Foundation of China (Nos. 52022054; 51974181); the Program for

 doi:10.20944/preprints202202.0040.v1

Professor of Special Appointment (Eastern Scholar) at Shanghai Institutions of Higher Learning (TP2019041).

Institutional Review Board Statement: Not applicable.

Informed Consent Statement: Not applicable.

Data Availability Statement: Available upon request.

Acknowledgments: We would like to thank the research group of Dr. Han Dong at the School of Materials Science and Engineering, Shanghai University for the support of optical microscopy. Thanks for the support of scanning electron microscopy provided by Shanghai Dianji University. Thanks to Ms. Cheng Biao, Humboldt University of Berlin for her language support. We also thanks to the anonymous reviewers of this paper for their constructive comments.

Conflicts of Interest: The authors declare no conflict of interest.

 doi:10.20944/preprints202202.0040.v1

Reference

[1] Wu, X., Review of alloy and process development of TiAl alloys. *Intermetallics* **2006,** *14* (10), 1114-1122.

[2] Dimiduk, D. M., Gamma titanium aluminide alloys—an assessment within the competition of aerospace structural materials. *Mater. Sci. Eng. A* **1999,** *263* (2), 281-288.

[3] Clemens, H.; Wallgram, W.; Kremmer, S.; Güther, V.; Otto, A.; Bartels, A., Design of Novel β-Solidifying TiAl Alloys with Adjustable β/B2-Phase Fraction and Excellent Hot-Workability. *Adv. Eng. Mater.* **2008,** *10* (8), 707-713.

[4] Clemens, H.; Mayer, S., Design, Processing, Microstructure, Properties, and Applications of Advanced Intermetallic TiAl Alloys. *Adv. Eng. Mater.* **2013,** *15* (4), 191-215.

[5] Hu, D., Effect of composition on grain refinement in TiAl-based alloys. *Intermetallics* **2001,** *9* (12), 1037-1043.

[6] Shida, Y.; Anada, H., The effect of various ternary additives on the oxidation behavior of TiAl in high-temperature air. *Oxid. Met.* **1996,** *45* (1), 197-219.

[7] Yoshihara, M.; Miura, K., Effects of Nb addition on oxidation behavior of TiAl. *Intermetallics* **1995,** *3* (5), 357-363.

[8] Güther, V.; Allen, M.; Klose, J.; Clemens, H., Metallurgical processing of titanium aluminides on industrial scale. *Intermetallics* **2018,** *103*, 12-22.

[9] Foroozmehr, A.; Kermanpur, A.; Ashrafizadeh, F.; Kabiri, Y., Effects of thermo-mechanical parameters on microstructure and mechanical properties of Ti-50 at.%Ni shape memory alloy produced by VAR method. *Mater. Sci. Eng. A* **2012,** *535*, 164-169.

[10] Mi, J.; Harding, R. A.; Wickins, M.; Campbell, J., Entrained oxide films in TiAl castings. *Intermetallics* **2003,** *11* (4), 377-385.

[11] Kim, Y. W.; Rosenberger, A.; Dimiduk, D. M., Microstructural changes and estimated strengthening contributions in a gamma alloy Ti–45Al–5Nb pack-rolled sheet. *Intermetallics* **2009,** *17* (12), 1017-1027.

[12] Gomes, F.; Barbosa, J.; Ribeiro, C. S., Induction melting of γ-TiAl in CaO crucibles. *Intermetallics* **2008,** *16* (11), 1292-1297.

[13] Lapin, J.; Gabalcová, Z.; Pelachová, T., Effect of Y2O3 crucible on contamination of directionally solidified intermetallic Ti–46Al–8Nb alloy. *Intermetallics* **2011,** *19* (3), 396-403.

[14] Subbarao, E. C.; Sutter, P. H.; Hrizo, J., Defect Structure and Electrical Conductivity of ThO2-Y2O3 Solid Solutions. *J. Am. Ceram. Soc.* **1965,** *48* (9), 443-446.

[15] Li, C. H.; He, J.; Wei, C.; Wang, H. B.; Lu, X. G., Solidification and Interface Reaction of Titanium Alloys in the BaZrO3 Shell-Mould. *Mater. Sci. Forum* **2015,** *828-829*, 106-111.

[16] Li, C. H.; Gao, Y. H.; Lu, X. G.; Ding, W. Z.; Ren, Z. M.; Deng, K., Interaction between the Ceramic CaZrO3 and the Melt of Titanium Alloys. Advances in Science and Technology 2011, 70, 136-140.

[17] Tetsui, T.; Kobayashi, T.; Ueno, T.; Harada, H., Consideration of the influence of contamination from oxide crucibles on TiAl cast material, and the possibility of achieving low-purity TiAl precision cast turbine wheels. *Intermetallics* **2012,** *31*, 274-281.

[18] Barbosa, J. J.; Ribeiro, C. S., Influence of crucible material on the level of contamination in TiAl using induction melting. *Int. J. Cast Met. Res.* **2000,** *12* (5), 293-301.

[19] Čegan, T.; Szurman, I.; Kursa, M.; Holesinsky, J.; Vontorova, J., Preparation of TiAl-based alloys by induction melting in graphite crucibles. *Kovove Materialy* **2015,** *53*, 69-78.

[20] Chapin, E.; Friske, W., Metallurgical Evaluation of Refractory Compounds for Containing Molten Titanium: I, Oxides. *Naval Research Lab. Rept.* **2015**.

[21] Kuang, J. P.; Harding, R. A.; Campbell, J., A study of refractories as crucible and mould materials for melting and casting γ-TiAl alloys. *Int. J. Cast Met. Res.* **2001,** *13* (5), 277-292.

[22] Chen, G.; Gao, P.; Kang, J.; Li, B.; Ali, W.; Qin, Z.; Lu, X.; Li, C., Improved stability of BaZrO3 refractory with Y2O3 additive and its interaction with titanium melts. *J. Alloys Compd.* **2017,** *726*, 403-409.

[23] Chen, G.; Lan, B.; Xiong, F.; Gao, P.; Zhang, H.; Lu, X.; Li, C., Pilot-scale experimental evaluation of induction melting of Ti-46Al-8Nb alloy in the fused BaZrO3 crucible. *Vacuum* **2019,** *159*, 293-298.

[24] Zhang, Z.; Zhu, K.; Liu, L.; Wu, G.; Chen, G., Preparation of BaZrO3 Crucible and Its Interfacial Reaction with Molten Titanium Alloys. *J. Chin. Ceram. Soc.* **2013,** *41*.

[25] Khalid, F.; Edmonds, D., The Processing, Properties and Applications of Metallic Ceramic Materials. *Proc. IRC Birmingham* **1992,** *2*.

[26] Blackburn, M. J.; Malley, D. R., Plasma arc melting of titanium alloys. *Mater. Des.* **1993,** *14* (1), 19-27.

[27] Hu, D.; Godfrey, A.; Blenkinsop, P. A.; Loretto, M. H., Processing-property-microstructure relationships in TiAl-based alloys. *Metall. Mater. Trans. A* **1998,** *29* (13), 919-925.

[28] Yanqing, S.; Jingjie, G.; Jun, J.; Guizhong, L.; Yuan, L., Composition control of a TiAl melt during the induction skull melting (ISM) process. *J. Alloys Compd.* **2002,** *334* (1), 261-266.

[29] Witusiewicz, V. T.; Bondar, A. A.; Hecht, U.; Velikanova, T. Y., The Al–B–Nb–Ti system: IV. Experimental study and thermodynamic re-evaluation of the binary Al–Nb and ternary Al–Nb–Ti systems. *J. Alloys Compd.* **2009,** *472* (1), 133-161.

[30] McCullough, C.; Valencia, J. J.; Levi, C. G.; Mehrabian, R., Phase equilibria and solidification in Ti-Al alloys. *Acta Metall.* **1989,** *37* (5), 1321-1336.

[31] Larsen, D. E.; kampe, S.; Christodoulou, L., Effect of XD™ TiB2 Volume Fraction on the Microstructure of a Cast Near-gamma titanium aluminide alloy. *MRS Online Proceedings Library* **1990,** *194* (1), 285-292.

[32] Imayev, R. M.; Imayev, V. M.; Oehring, M.; Appel, F., Alloy design concepts for refined gamma titanium aluminide based alloys. *Intermetallics* **2007,** *15* (4), 451-460.

[33] Zollinger, J.; Lapin, J.; Daloz, D.; Combeau, H., Influence of oxygen on solidification behaviour of cast TiAl-based alloys. *Intermetallics* **2007,** *15* (10), 1343-1350.

[34] Saage, H.; Huang, A. J.; Hu, D.; Loretto, M. H.; Wu, X., Microstructures and tensile properties of massively transformed and aged Ti46Al8Nb and Ti46Al8Ta alloys. *Intermetallics* **2009,** *17* (1), 32-38.

[35] Xiao, S.; Guo, Y.; Liang, Z.; Wang, X.; Yang, J.; Wang, X.; Xu, L.; Tian, J.; Chen, Y., The effect of nano-Y2O3 addition on tensile properties and creep behavior of as-cast TiAl alloy. *J. Alloys Compd.* **2020,** *825*, 153852.

[36] Liu, Y.; Liang, X.; Liu, B.; He, W.; Li, J.; Gan, Z.; He, Y., Investigations on processing powder metallurgical high-Nb TiAl alloy sheets. *Intermetallics* **2014,** *55*, 80-89.